International Journal of Solids and Structures 171 (2019) 181–188

Contents lists available at ScienceDirect

International Journal of Solids and Structures

journal homepage: www.elsevier.com/locate/ijsolstr

Designing tunable composites with general interfaces

S. Saeb[a], P. Steinmann[a,b], A. Javili[c,*]

[a] Chair of Applied Mechanics, University of Erlangen–Nuremberg, Egerland Str. 5, Erlangen 91058, Germany
[b] School of Engineering, University of Glasgow, Glasgow G12 8QQ, United Kingdom
[c] Department of Mechanical Engineering, Bilkent University, Ankara 06800, Turkey

ARTICLE INFO

Article history:
Received 7 October 2018
Revised 27 March 2019
Available online 10 April 2019

Keywords:
Smart materials
Interface/interphase
Computational modeling
Micro-mechanics
Size-effect
Composites

ABSTRACT

In this manuscript, we employ interface enhanced computational homogenization to explore and detail on a number of unfamiliar characteristics that composites can exhibit at different length scales. Here, the interface between the constituents is general in the sense that both displacement and traction jumps across the interface are admissible. We carry out numerous computational investigations using the finite element method for a broad range of various material parameters. Our numerical results reveal that the effective response of a microstructure embedding general interfaces is intuitively unpredictable and highly complex. In particular, for certain ranges of material parameters the overall response shows insensitivity with respect to either microstructure size or stiffness-ratio between inclusion and matrix. This unique behavior is observed likewise for two- and three-dimensional unit-cells. Our findings provide a valuable guideline to design tunable composites utilizing interfaces.

1. Introduction

During the last decades, composites have drawn research attention due to their superior physical properties and great flexibility. These multifunctional materials have proven as promising alternatives to conventional materials in a variety of applications ranging from medical to engineering industry. In order to understand the behavior of composites at different length scales, two key aspects shall be considered. On the one hand, the response of a heterogeneous material such as a composite stems from its underlying microstructure and therefore predicting the response of composites is tightly linked to understanding the behavior of their microstructures. On the other hand, most of the materials exhibit unfamiliar behavior at small scales mainly due to considerably larger surface/interface-to-volume ratio. Thus, modeling the behavior of composites requires understanding the behavior of their microstructures at a broad length scale spectrum and particularly at small scales.

In order to take the influence of the underlying microstructure into account, several multi-scale models have been developed in the past. Among these methods, the homogenization technique pioneered by Hill (1972) has gained lots of interest. The main objective of homogenization is to estimate the effective macroscopic properties of a heterogeneous material from the response of its microstructure, thereby allowing to substitute the heterogeneous material with an equivalent homogeneous one. One of the key ingredients of homogenization is the scale separation, which assumes that the microstructure of the composite material is far smaller than the characteristic length of the macrostructure. This assumption allows for separating the problem into two coupled micro- and macro-scales. The sample at the micro-scale is commonly referred to as the RVE, see Drugan and Willis (1996); Kanit et al. (2003); Ostoja-Starzewski (2006); Pindera et al. (2009); Jafari et al. (2011); Bargmann et al. (2018) for further details. Another key ingredient of homogenization is the the virtual power equivalence between the scales known as the Hill–Mandel condition (Hill, 1963). This condition is fulfilled by imposing appropriate boundary conditions onto the micro-problem. Homogenization methods are generally subdivided into analytical and computational methods. Analytical models have progressively been developed during the last years and are now capable of predicting the behavior of certain composites, see Ponte Castañeda (1992); Mura et al. (1996); Nemat-Nasser and Hori (1999); Charalambakis (2010); Klusemann et al. (2012); Tsalis et al. (2012) among others. However, they generally fail to provide accurate results for complex structures. In order to resolve this shortcoming, computational homogenization was developed. For instance, in the commonly used FE^2 technique, the finite element method is employed to solve the micro- and

* Corresponding author.
E-mail addresses: saba.saeb@fau.de (S. Saeb), paul.steinmann@fau.de (P. Steinmann), ajavili@bilkent.edu.tr (A. Javili).

https://doi.org/10.1016/j.ijsolstr.2019.04.006
0020-7683/

macro-problems concurrently (Feyel, 1999; Miehe, 2002; Drago and Pindera, 2007; Temizer and Wriggers, 2011; Schröder and Keip, 2012; Javili et al., 2013; Eidel and Fischer, 2018), see also Moës et al. (2003); Cavalcante et al. (2011); Savvas et al. (2014); Kochmann et al. (2017) for details on other computational methods. Detailed reviews of computational homogenization can be found in Saeb et al. (2016); Matouš et al. (2017).

Although computational homogenization is a powerful tool to model the behavior of composite materials, it lacks a physical length scale and as a result fails to account for size-dependent response of materials referred to as *size-effect*. Such a size-dependent behavior is caused by larger interface-to-volume ratio at smaller scales. Motivated by this justification, several authors showed that the size-dependent response can be captured by approximating the finite thickness interphase between the phases with a zero-thickness mathematical model, termed "interface" (Quang and He, 2007; Yvonnet et al., 2008a; Fritzen and Leuschner, 2015; Maleki Moghadam et al., 2016; Ansari and Gholami, 2016; Wilmers et al., 2017; Chen et al., 2018), see also Cordero et al. (2016). It is usually assumed that interfaces possess their own energetic structure different from the bulk. Interfaces may be assigned to different groups depending on the jump condition of certain fields across the interface. For mechanical problems, depending on the jump conditions for the displacement and the traction field, interfaces can be categorized as *perfect, elastic, cohesive* and *general* interface. The perfect interface model is the simplest type of interfaces and assumes a continuous displacement and traction field across the interface. The elastic interface model, which can be viewed as an extension of surface elasticity theory (Gurtin and Murdoch, 1975; Park et al., 2006; He and Lilley, 2008; Altenbach and Eremeyev, 2017; Chen et al., 2018), allows for a traction jump across the interface while it is valid only for coherent interfaces. On the other hand, the cohesive interface model (Xu and Needleman, 1994; Ortiz and Pandolfi, 1999; Park and Paulino, 2013) does not allow for a traction jump across the interface, but permits opening of the interface, thus making it suitable for modeling of material failure. The general interface model can be viewed as a comprehensive interface description allowing for both, traction and displacement jumps across the interface. Various aspects of the general interface model for mechanical and thermal problems have been discussed in Hashin (2002); Duan and Karihaloo (2007); Pavanello et al. (2012); Javili et al. (2014); Javili (2017) among others. Incorporation of elastic and cohesive interfaces into a computational homogenization framework has been investigated thoroughly in the literature (Yvonnet et al., 2008b; Brassart et al., 2009; Tran et al., 2016). Recently, computational homogenization accounting for general interfaces is studied in Javili et al. (2017). Javili et al. (2017) have shown that including general interfaces results in a complex and highly non-linear size-effect, which may be understood as the intricate combination of smaller-stronger and smaller-weaker responses associated with the elastic and cohesive contributions, respectively. Their numerical results are compared against the analytical solution in Chatzigeorgiou et al. (2017) and a perfect agreement is reported.

Although the theoretical and computational aspects of computational homogenization accounting for general interfaces have been well established, the associated physical characteristics of the general interface remained less understood, mainly due to the limited scope of the numerical investigations. The main objective of this manuscript is to reveal and detail on some unprecedented features of the general interface model in view of computational homogenization. To do so, we briefly review the necessary computational aspects of the framework developed in Javili et al. (2017); Chatzigeorgiou et al. (2017). Afterwards, the response of materials in the presence of general interfaces is investigated through numerous examples.

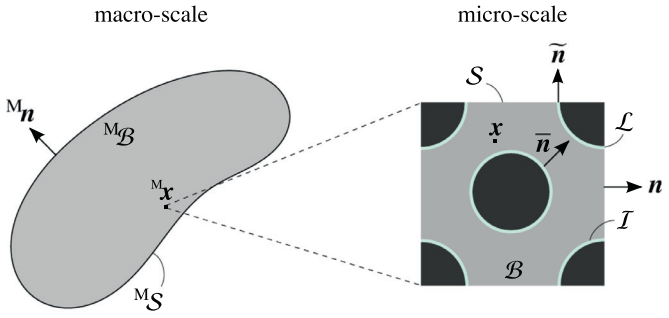

Fig. 1. Graphical summary of computational homogenization accounting for interfaces at the micro-level. The material configuration $\mathcal{B}$ corresponds to a RVE which includes the geometrical information of a macroscopic point. The local macroscopic response is obtained through solving the associated boundary value problem at the micro-scale and averaging theorems.

The key features presented in this manuscript are as follows. Firstly, we show that the size-effect due to the general interface model can switch from commonly accepted smaller-stronger to smaller-weaker depending on the size and inclusion to matrix stiffness-ratio. Yet the overall response obtained from the general interface model remains bounded by those associated with cohesive and elastic interface models. Secondly, we demonstrate that there exists a *critical size* where the effective response no longer depends on the *stiffness-ratio*. Analogously, for a *critical stiffness-ratio*, the effective response does not depend on the *size*. Moreover, for a *critical set of interface parameters*, the effective response shows no sensitivity to volume fraction. Thirdly, analytical estimates for the critical length-ratio and critical stiffness-ratio are derived that are in excellent agreement with the computational simulations using the finite element method. Finally, the generality of the results is demonstrated by carrying out simulations on a three-dimensional unit-cell and a microstructure with randomly distributed inclusions. We believe that the aforementioned features along with the following discussions shed light on the enormous potential of general interfaces to design tunable composites and multifunctional materials.

2. Theory

The primary goal of this section is to review the theoretical aspects of modeling the behavior of a RVE accounting for general interfaces in a computational homogenization framework. First, the kinematic relations and governing equations of the problem are discussed. This is then followed by presenting principal aspects of computational homogenization. In particular, proper volume averaging techniques to relate macroscopic and microscopic quantities are given. Moreover, the extended form of the Hill–Mandel condition accounting for the general interface model is presented. This work is based on the first-order strain-driven computational homogenization, meaning that the macroscopic strain $^{\mathrm{M}}\boldsymbol{\varepsilon}$ is the input for the micro-problem and the macroscopic stress $^{\mathrm{M}}\boldsymbol{\sigma}$ is sought.

Consider a continuum body at the macro-scale representing a heterogeneous material that occupies the configuration $^{\mathrm{M}}\mathcal{B}$, as shown in Fig. 1. The inhomogeneities within the material are separated from the matrix via a finite-thickness interphase. These interphases are modeled with the zero-thickness general interface model at the micro-scale. Therefore, the interphase/interface effects enter the macro-problem only implicitly but are explicitly included at the micro-scale. The configuration $\mathcal{B}$ at the micro-scale with coordinates $\boldsymbol{x}$ represents the RVE of the heterogeneous material. The external boundary of the RVE is denoted $\mathcal{S}$. The outward unit normals to $\mathcal{S}$ is denoted $\boldsymbol{n}$. The configuration $\mathcal{B}$ consists of two

disjoint subdomains, $\mathcal{B}^+$ and $\mathcal{B}^-$ bonded together at the interface $\mathcal{I}$. The boundary of the interface $\mathcal{I}$ is denoted $\mathcal{L}$ whose outward unit normal is denoted $\widetilde{\boldsymbol{n}}$. The interface unit normal is presented by $\overline{\boldsymbol{n}}$ and points from the minus to the plus side of the interface. The displacement within the bulk is $\boldsymbol{u} = \boldsymbol{u}(\boldsymbol{x})$. Analogously, the displacements on two sides of the interfaces are denoted $\boldsymbol{u}^+$ and $\boldsymbol{u}^-$. A crucial assumption made here is that the displacement of the interface is not arbitrary and evaluated as $\overline{\boldsymbol{u}} = \{\{\boldsymbol{u}\}\} := \frac{1}{2}[\boldsymbol{u}^+ + \boldsymbol{u}^-]$. The strains in the bulk and within the interface are defined by

$$\begin{aligned}\boldsymbol{\varepsilon} &= \frac{1}{2}\Big[[\mathrm{grad}\boldsymbol{u}] + [\mathrm{grad}\boldsymbol{u}]^{\mathrm{t}}\Big] \quad \text{in} \quad \mathcal{B},\\ \overline{\boldsymbol{\varepsilon}} &= \frac{1}{2}\Big[\overline{\boldsymbol{i}}\cdot[\mathrm{grad}\,\overline{\boldsymbol{u}}]\cdot\overline{\boldsymbol{i}} + \overline{\boldsymbol{i}}\cdot[\mathrm{grad}\,\overline{\boldsymbol{u}}]^{\mathrm{t}}\cdot\overline{\boldsymbol{i}}\Big] \quad \text{on} \quad \mathcal{I},\end{aligned} \tag{1}$$

respectively, in which $\overline{\boldsymbol{i}} = \boldsymbol{i} - \overline{\boldsymbol{n}}\otimes\overline{\boldsymbol{n}}$ is the interface projection tensor and "grad{•}" denotes the gradient operator with $\{\bullet\}^{\mathrm{t}}$ being the transpose operator. The governing equations of the problem at the micro-scale are the balance of linear momentum in the bulk and on the interface as Javili et al. (2017); Chatzigeorgiou et al. (2017)

$$\mathrm{div}\,\boldsymbol{\sigma} = \boldsymbol{0} \quad \text{in}\,\mathcal{B} \quad \text{subject to} \quad \boldsymbol{\sigma}\cdot\boldsymbol{n} = \boldsymbol{t} \quad \text{on}\,\mathcal{S}, \tag{2}$$

$$\begin{aligned}&\mathrm{grad}\overline{\boldsymbol{\sigma}} : \overline{\boldsymbol{i}} + [\![\boldsymbol{\sigma}]\!]\cdot\overline{\boldsymbol{n}} = \boldsymbol{0} \quad \text{on}\,\mathcal{I}\\ &\text{subject to} \quad \{\{\boldsymbol{\sigma}\}\}\cdot\overline{\boldsymbol{n}} = \{\{\boldsymbol{t}\}\} \ \text{across}\,\mathcal{I} \quad \text{and} \quad \overline{\boldsymbol{\sigma}}\cdot\widetilde{\boldsymbol{n}} = \widetilde{\boldsymbol{t}} \ \text{on}\,\mathcal{L},\end{aligned} \tag{3}$$

where $\boldsymbol{\sigma}$ and $\overline{\boldsymbol{\sigma}}$ denote the stresses in the bulk and within the interface, respectively. Moreover, $[\![\boldsymbol{\sigma}]\!]\cdot\overline{\boldsymbol{n}}$ represents the traction jump as $[\![\boldsymbol{\sigma}]\!]\cdot\overline{\boldsymbol{n}} = [\boldsymbol{\sigma}^+ - \boldsymbol{\sigma}^-]\cdot\overline{\boldsymbol{n}}$ where $\boldsymbol{\sigma}^+$ and $\boldsymbol{\sigma}^-$ represent the stresses on $\mathcal{B}^+$ and $\mathcal{B}^-$, respectively.

In order to proceed, we specify the material behavior of the bulk and the interface. The material behavior of the bulk takes the standard elastic and isotropic response as $\boldsymbol{\sigma} = 2\mu\,\boldsymbol{\varepsilon} + \lambda\,[\boldsymbol{\varepsilon} : \boldsymbol{i}]\,\boldsymbol{i}$ in which μ and λ are the Lamé parameters and related to the bulk modulus via $\kappa = 2\mu/3 + \lambda$. Moreover, the operator ":" denotes the standard double contraction. We additively decompose the behavior of the interface into to a tangential part associated to the elastic interface model and an orthogonal part representing the cohesive interface model. The response of the material along the interface takes the form $\overline{\boldsymbol{\sigma}} = 2\,\overline{\mu}\,\overline{\boldsymbol{\varepsilon}} + \overline{\lambda}\,[\overline{\boldsymbol{\varepsilon}} : \overline{\boldsymbol{i}}]\,\overline{\boldsymbol{i}}$ where $\overline{\mu}$ and $\overline{\lambda}$ denote the elastic interface material parameters. In a two-dimensional setting and within the scope of this contribution, the interface is a one-dimensional manifold resisting against stretch. Therefore, it is sufficient to introduce only one material parameter to define the elastic behavior along the interface and therefore we set $\overline{\lambda} = 0$ for two-dimensional examples. In a three-dimensional setting, the interface is a two-dimensional manifold resisting against shear as well as expansion deformations giving rise to non-zero values for both $\overline{\mu}$ and $\overline{\lambda}$. It is also possible to account for flexural resistance of the elastic interface as discussed in Steigmann and Ogden (1999), see also Han et al. (2018). The behavior of the material across the interface is assumed to be governed by the traction-separation law $\{\{\boldsymbol{t}\}\} = \overline{k}[\![\boldsymbol{u}]\!]$ in which $\overline{k}$ denotes the cohesive parameter.

Next, macroscopic quantities are related to their microscopic counterparts through employing a proper micro-to-macro transition technique. As discussed in Chatzigeorgiou et al. (2017), when general interfaces are taken into account, the macroscopic strain and stress are defined through

$$\begin{aligned}{}^{\mathrm{M}}\boldsymbol{\varepsilon} &= \frac{1}{\mathscr{V}}\int_{\mathcal{B}}\boldsymbol{\varepsilon}\,\mathrm{d}V + \frac{1}{\mathscr{V}}\int_{\mathcal{I}}\frac{1}{2}[\,[\![\boldsymbol{u}]\!]\otimes\overline{\boldsymbol{n}} + \overline{\boldsymbol{n}}\otimes[\![\boldsymbol{u}]\!]\,]\,\mathrm{d}A\\ &= \frac{1}{\mathscr{V}}\int_{\mathcal{S}}\frac{1}{2}[\boldsymbol{u}\otimes\boldsymbol{n} + \boldsymbol{n}\otimes\boldsymbol{u}]\,\mathrm{d}A,\end{aligned} \tag{4}$$

$${}^{\mathrm{M}}\boldsymbol{\sigma} = \frac{1}{\mathscr{V}}\int_{\mathcal{B}}\boldsymbol{\sigma}\,\mathrm{d}V + \frac{1}{\mathscr{V}}\int_{\mathcal{I}}\overline{\boldsymbol{\sigma}}\,\mathrm{d}A = \frac{1}{\mathscr{V}}\int_{\mathcal{S}}\boldsymbol{t}\otimes\boldsymbol{x}\,\mathrm{d}A + \frac{1}{\mathscr{V}}\int_{\mathcal{L}}\widetilde{\boldsymbol{t}}\otimes\overline{\boldsymbol{x}}\,\mathrm{d}L\,, \tag{5}$$

respectively, in which $\mathscr{V}$ is the total volume of the microstructure. The dyadic product $\otimes$ of two vectors $\boldsymbol{a}$ and $\boldsymbol{b}$ is a second-order tensor $\boldsymbol{C}$ with components $C_{ij} = a_i b_j$. Finally, the equivalence of the virtual power across the scales shall be guaranteed through the Hill–Mandel condition. This reads

$$\underbrace{\underbrace{\frac{1}{\mathscr{V}}\int_{\mathcal{B}}\boldsymbol{\sigma} : \delta\boldsymbol{\varepsilon}\,\mathrm{d}V}_{\text{bulk}} + \underbrace{\frac{1}{\mathscr{V}}\int_{\mathcal{I}}\overline{\boldsymbol{\sigma}} : \delta\overline{\boldsymbol{\varepsilon}}\,\mathrm{d}A}_{\text{along the interface}} + \underbrace{\frac{1}{\mathscr{V}}\int_{\mathcal{I}}\{\{\boldsymbol{t}\}\}\cdot[\![\delta\boldsymbol{u}]\!]\,\mathrm{d}A}_{\text{across the interface}}}_{\text{micro-scale}} - \underbrace{{}^{\mathrm{M}}\boldsymbol{\sigma} : \delta^{\mathrm{M}}\boldsymbol{\varepsilon}}_{\text{macro-scale}} \doteq 0\,. \tag{6}$$

In this manuscript, we assume that $\mathcal{L} = \emptyset$ meaning that the interface does not penetrate the boundary of the microstructure. It can be shown (Javili et al., 2017) that under such assumption condition (6) can be expressed in terms of boundary integrals as follows

$$\frac{1}{\mathscr{V}}\int_{\mathcal{S}}[\delta\boldsymbol{u} - \delta^{\mathrm{M}}\boldsymbol{\varepsilon}\cdot\boldsymbol{x}]\cdot\boldsymbol{t} \doteq 0\,. \tag{7}$$

This format is particularly convenient as admissible boundary conditions to be imposed on the RVE can be readily derived. The canonical constraints that sufficiently satisfy the Hill–Mandel condition are displacement, periodic and traction boundary conditions. In this manuscript, we only employ periodic boundary conditions to solve the boundary value problem at the micro-scale bearing in mind that displacement and traction boundary conditions provide overestimated and underestimated responses, respectively. Upon choosing the boundary condition, the governing equations (2) and (3) can be solved through a proper computational technique. Presenting the details regarding the computational aspects of the solution procedure is out of the scope of this manuscript but can be found in Javili et al. (2017).

3. Numerical observations: Towards designing tunable composites

This section details on a number of distinctive features that the general interface model exhibits in the context of computational homogenization. In particular, we study the change in the effective response with respect to the length-ratio ℓ (size), the inclusion to matrix stiffness-ratio $\mathcal{R}$ and the interface material parameters $\overline{\mu}$, $\overline{k}$. Fig. 2 illustrates the link between the size of the samples and the length-ratio ℓ. Changing the size is realized by scaling the dimensions of the reference unit-cell according to ℓ. In this manuscript, we investigate only the case that the microstructure undergoes volumetric expansion and therefore focus on the effective bulk modulus ${}^{\mathrm{M}}\kappa$ as the effective response. The material parameters of the matrix are fixed as $\mu = 8$ and $\kappa = 20$ for all numerical examples. The inclusion material parameters vary though and are scaled through $\mathcal{R}$. For instance, when $\mathcal{R}$ is set to 0.1, the inclusion is 10 times more compliant than the matrix with $\mu = 0.8$ and $\kappa = 2$ and when it is set to 10, the inclusion is 10 times stiffer than the matrix with $\mu = 80$ and $\kappa = 200$. Obviously, interface material parameters govern the behavior of the material along and across the interface. For example, when $\overline{k} \to \infty$, the interface remains coherent and cannot open. On the other hand, when $\overline{k} \to 0$, the interface shows no resistance against opening. Similarly, large and small values of $\overline{\mu}$ identify high- and low-resistant response in the tangential direction, respectively. The majority of the numerical studies are conducted on a two-dimensional unit-cell with volume fraction of $f = 25\%$. However, in order to demonstrate the

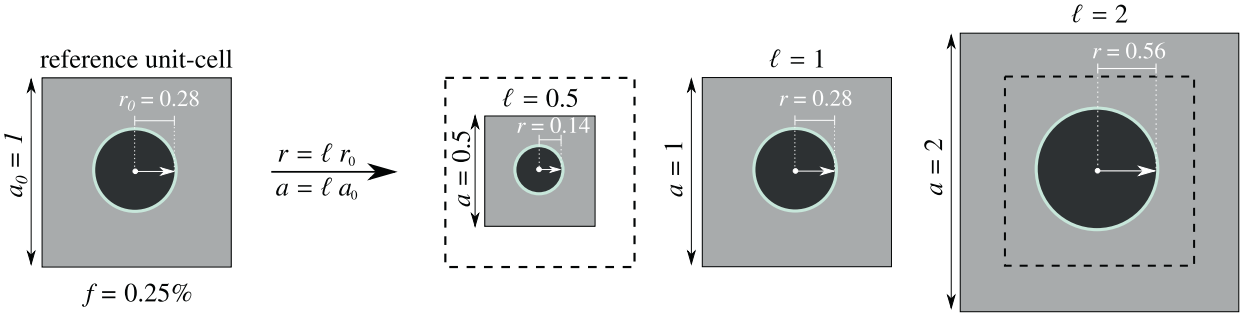

Fig. 2. The size of the unit-cells change based on a reference unit-cell and according to the length-ratio ℓ. The inclusion volume fraction remains the same $f = 0.25\%$ for all the unit-cells.

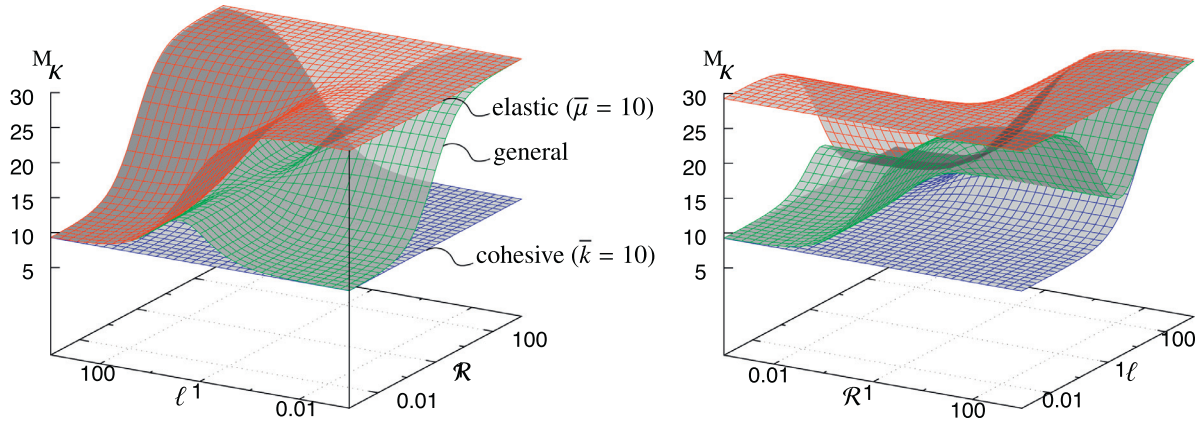

Fig. 3. Effective bulk modulus with varying the length-ratio and the inclusion to matrix stiffness-ratio. The two plots depict the same results from different viewpoints. Different surfaces represent the results of various interface models. The results from the general interface model remain bounded by the elastic interface from the top and by the cohesive interface from the bottom.

extendibility of our findings, we carry out two sets of numerical studies on a three-dimensional unit-cell and a two-dimensional microstructure with random distribution of particles. All the simulations are performed using our in-house finite element code.

First, we compare the change in the effective response of three different microstructures for various values of $\ell \in [0.002, 500]$ and $\mathcal{R} \in [0.002, 500]$. The microstructures differ in the interface type embedded between the inclusion and the matrix which are, respectively, elastic, cohesive and general interfaces. Interface material parameters are set to $\overline{\mu} = 10$ and $\overline{k} = 10$. Clearly, $\overline{k} \to \infty$ and $\overline{\mu} \to 0$ for elastic and cohesive interfaces, respectively. This study is performed on the two-dimensional unit-cell. The numerical results depicted in Fig. 3 indicate that elastic and cohesive interfaces yield, in general, either a smaller-stronger or a smaller-weaker response, respectively. Exceptions can be found in two extreme values of $\mathcal{R}$, though. That is, when $\mathcal{R}$ is very small, the inclusion is essentially replaced by a void. Therefore, the interface may not resist against opening and the cohesive interface model is deactivated making the effective response insensitive to the size. On the other hand, when $\mathcal{R}$ is very large, the inclusion is replaced by a rigid particle. Under such condition, the length of the interface may not vary leading to eliminating the elastic interface effect and thus the effective response becomes size independent. Additionally, it is observed that the elastic and the cohesive interfaces yield, in general, a stiffer response as $\mathcal{R}$ increases. Once again, exceptions can be found for extreme values of ℓ. That is, when ℓ is very large, interface effects are negligible and consequently, elastic and cohesive interfaces recover the results from the perfect interface model. On the other hand, when ℓ is very small, interface effects are significant and elastic and cohesive interfaces, regardless of $\mathcal{R}$, recover the response of a microstructure with a rigid inclusion and a microstructure with a void at its center, respectively. Taken together, it can be concluded that the change in the effective response obtained from the elastic and the cohesive interface model with respect to either ℓ or $\mathcal{R}$ is monotonic and intuitively predictable. This is not the case for the general interface though. The numerical results confirm that the change in the effective response from the general interface is highly non-linear, relatively complex and not at all intuitively predictable. In particular, the size-effect captured by the general interface model switches from a smaller-stronger to a smaller-weaker response and vice versa depending on the values of ℓ and $\mathcal{R}$. Moreover, in contrast to the other two interface types, the response obtained from the general interface model becomes insensitive to the change in $\mathcal{R}$ for a relatively moderate value of ℓ. We emphasize that this behavior is specific to the general interface model and is distinct from what is observed for elastic and cohesive interface models. Clearly, such a complicated characteristic opens up the potential to consider general interfaces as proper tools to tailor-make materials or to design composites exhibiting unique behavior.

In order to better understand the complex behavior resulting from general interfaces, we perform a similar study only for the general interface model and for different combinations of interface material parameters. The numerical results depicted in Fig. 4 show that for all sets of interface material parameters, when $\mathcal{R}$ is small and within range B_1, the general interface model yields a smaller-stronger behavior for sizes in the range A_1 and switches to a smaller-weaker response for smaller sizes within the range A_2. An opposite behavior is observed for the case that $\mathcal{R}$ is larger and within the range B_2. Obviously, the ranges vary depending on the

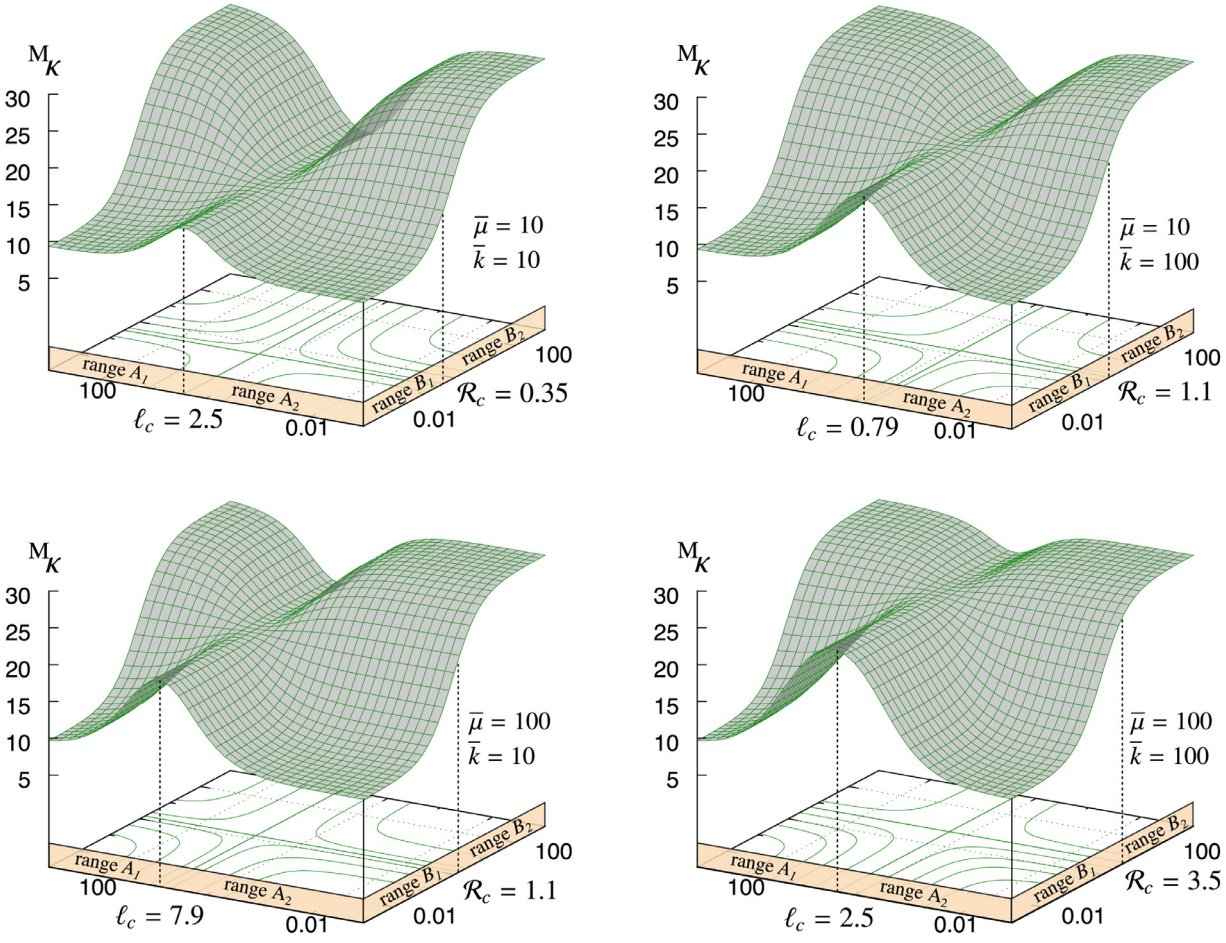

Fig. 4. Effective bulk modulus obtained from the general interface model with varying the length-ratio and the inclusion to matrix stiffness-ratio for several combinations of interface material parameters $\overline{\mu}$ and $\overline{k}$. The intersection point of ranges A_1 and A_2 identifies ℓ_c and the intersection point of ranges B_1 and B_2 identifies $\mathcal{R}_c$. The contour lines indicate that when $\ell = \ell_c$, changing $\mathcal{R}$ does not influence the effective response. Likewise, when $\mathcal{R} = \mathcal{R}_c$, changing ℓ does not influence the effective response.

interface material parameters. Having a closer look at these ranges reveals two interesting points and sheds light on unique characteristics of the general interface model. Firstly, the intersection of the ranges A_1 and A_2 identifies the *critical length-ratio* ℓ_c for which changing $\mathcal{R}$ does not influence the effective response. Secondly, the intersection of the ranges B_1 and B_2 identifies the *critical stiffness-ratio* $\mathcal{R}_c$ for which the effective bulk modulus becomes insensitive to ℓ. From another point of view, one could take advantage of these two points to detect the ranges of ℓ and $\mathcal{R}$ where the size-effect captured by the general interface model remains either smaller-stronger or smaller-weaker.

In order to identify the critical points more accurately and to better interpret the results, two side views of the plots are presented in Fig. 5. The numerical results indicate that ℓ_c, when $\overline{\mu} = 10$ and $\overline{k} = 10$, is equal to ℓ_c, when $\overline{\mu} = 100$ and $\overline{k} = 100$. Moreover, when $\overline{\mu} = 10$ and $\overline{k} = 100$, ℓ_c is 10 times smaller than the case that $\overline{\mu} = 100$ and $\overline{k} = 10$. These facts suggest that ℓ_c is a function of the ratio between the interface material parameters. On the other hand, it is observed that $\mathcal{R}_c$, when $\overline{\mu} = 10$ and $\overline{k} = 100$, is equal to $\mathcal{R}_c$, when $\overline{\mu} = 100$ and $\overline{k} = 10$. In addition, when $\overline{\mu} = 10$ and $\overline{k} = 10$, $\mathcal{R}_c$ is 10 times smaller than the case that $\overline{\mu} = 100$ and $\overline{k} = 100$. These facts also suggest that $\mathcal{R}_c$ is a function of the multiplication of the interface material parameters. Clearly, finding explicit relations for these two critical points in terms of parameters which are not a priori known requires running a significant number of numerical simulations. In order to circumvent this issue, we employ the analytical solution given in Chatzigeorgiou et al. (2017) for the effective bulk modulus of a circular microstructure that reads

$$^{\mathrm{M}}\kappa = \kappa_m + \frac{f}{\chi} \quad \text{with} \quad \chi = \frac{1}{\kappa_m \mathcal{R}\,\psi - \kappa_m + \omega\,[1+\psi]} + \frac{1-f}{\kappa_m + \mu_m}\,, \tag{8}$$

in which

$$\omega = \frac{\overline{\mu}}{2r} \quad , \quad \phi = \overline{k} r \quad , \quad \psi = \frac{\phi - \omega}{2\,\kappa_m\,\mathcal{R} + \phi + \omega}\,,$$

the subscripts i and m represent quantities related to the inclusion and the matrix, f denotes the inclusion volume fraction and r represents the radius of the inclusion. In order to find the critical points ℓ_c and $\mathcal{R}_c$, we take the derivatives of Eq. (8) with respect to $\mathcal{R}$ and ℓ, respectively, and set them equal to zero. With the aid of some mathematical reformulations and assuming a constant volume fraction, the critical points are obtained as

$$\frac{\partial\,^{\mathrm{M}}\kappa}{\partial \mathcal{R}} \doteq 0 \quad \Rightarrow \quad r_c = \sqrt{\frac{\overline{\mu}}{2\overline{k}}} \quad \Rightarrow \quad \ell_c = \sqrt{\frac{\overline{\mu}}{2r_0^2\overline{k}}} \quad ,$$

$$\frac{\partial\,^{\mathrm{M}}\kappa}{\partial \ell} \doteq 0 \quad \Rightarrow \quad \mathcal{R}_c = \sqrt{\frac{\overline{k}\,\overline{\mu}}{2{\kappa_m}^2}}, \tag{9}$$

in which r_0 is the radious of the reference unit-cell according to Fig. 2. The analytical solutions fully explain the results given in Fig. 5. In line with our numerical observations, ℓ_c and $\mathcal{R}_c$ are functions of the interface material parameters. Note that the

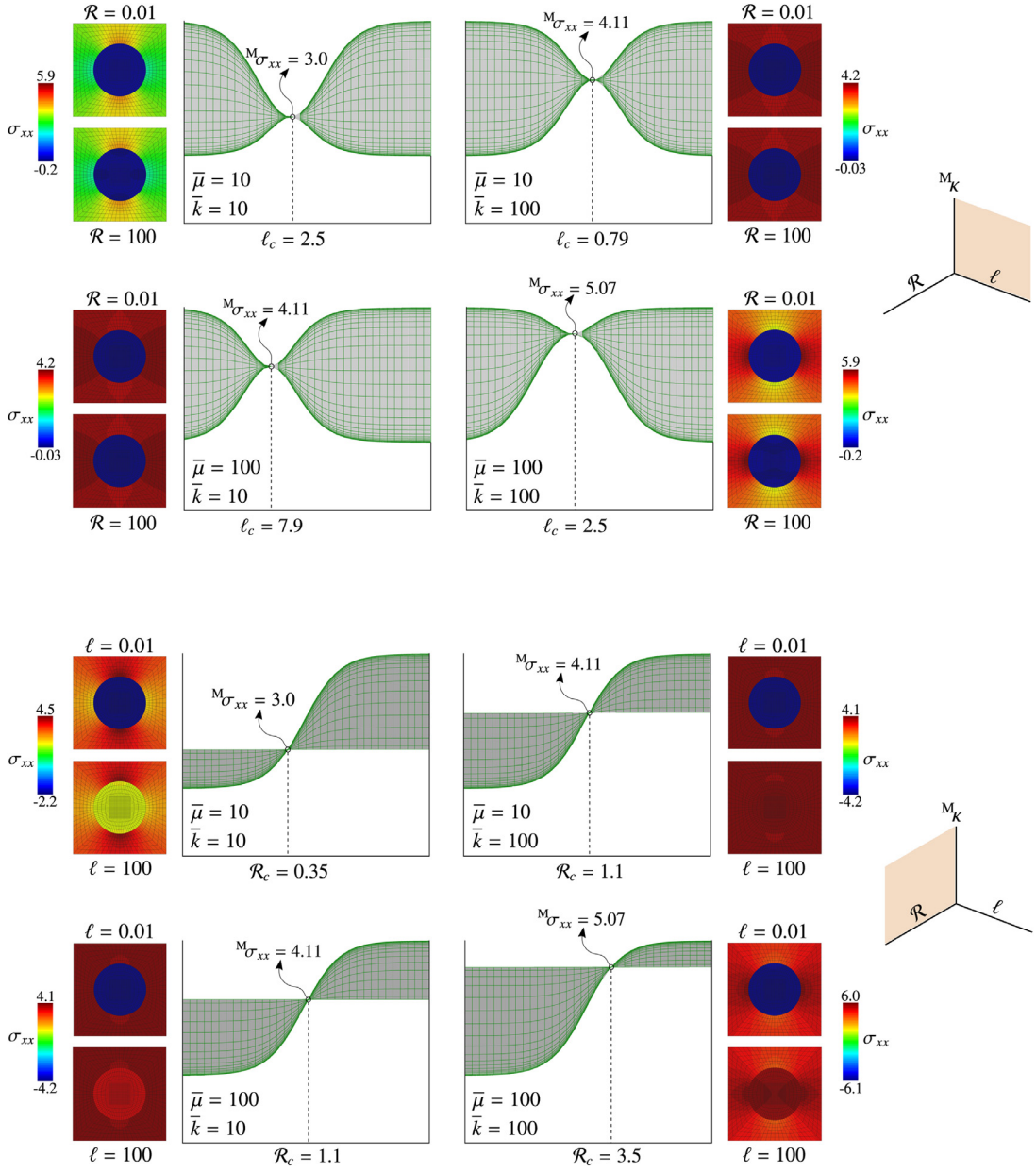

Fig. 5. Side views of Fig. 4. The figures next to the plot depict the distribution of *xx*-component of the Cauchy stress within the unit-cell for different values of $\mathcal{R}$ when $\ell = \ell_c$ (top) and different values of ℓ when $\mathcal{R} = \mathcal{R}_c$ (bottom). As can be seen, for $\ell = \ell_c$, the distributions remain the same regardless of $\mathcal{R}$. However, for $\mathcal{R} = \mathcal{R}_c$, the local response within the unit-cell varies depending on ℓ, but, the effective response remains unchanged.

critical length-ratio ℓ_c, in addition to the interface material parameters, depends solely on the radius of the inclusion in the reference unit-cell and surprisingly, not on the bulk material parameters. On the other hand, the critical stiffness-ratio $\mathcal{R}_c$, in addition to the interface material parameters, depends only on the matrix material parameters. It is worth emphasizing that the unique features of the general interface are not restricted to these two critical points and one could potentially further explore and discover similar points. As an additional example, we show in Fig. 6 that, for fixed values of $\mathcal{R}$, $\bar{k}$ and ℓ, one might find a particular value of $\bar{\mu}$ that results in the same effective response for unit-cells with inclusion volume fractions of $f = 15\%$ and $f = 35\%$. In particular, when $\mathcal{R} = 0.1$, $\bar{k} = 100$, $\ell = 1$ and $\mathcal{R} = 10$, $\bar{k} = 10$, $\ell = 1$, the *critical interface material parameters* are $\bar{\mu}_c = 10$ and $\bar{\mu}_c = 34$, respectively. Thus, tuning the general interface material parameters also allows for reduction of the inclusion proportion in the composite without losing the overall mechanical performance. Such numerical studies provide further relevant information for material scientists to take advantage of general interfaces to design materials based on their needs.

In order to demonstrate the generality of our findings, a similar computational study is carried out for a three-dimensional unit-cell and a two-dimensional microstructure with random distribution of inclusions as depicted in Fig. 7. Once again, the results show that the size-effect captured by the general interface model is quite complex and depending on $\mathcal{R}$ and ℓ, either smaller-stronger or smaller-weaker response may be observed. Overall, the trend of the results remain quite close to what is observed for the two-dimensional unit-cell. In particular, for both samples, there seems to exist a size in which the effective response remains constant regardless of the inclusion to matrix stiffness-ratio $\mathcal{R}$. Analogously, for a particular inclusion to matrix

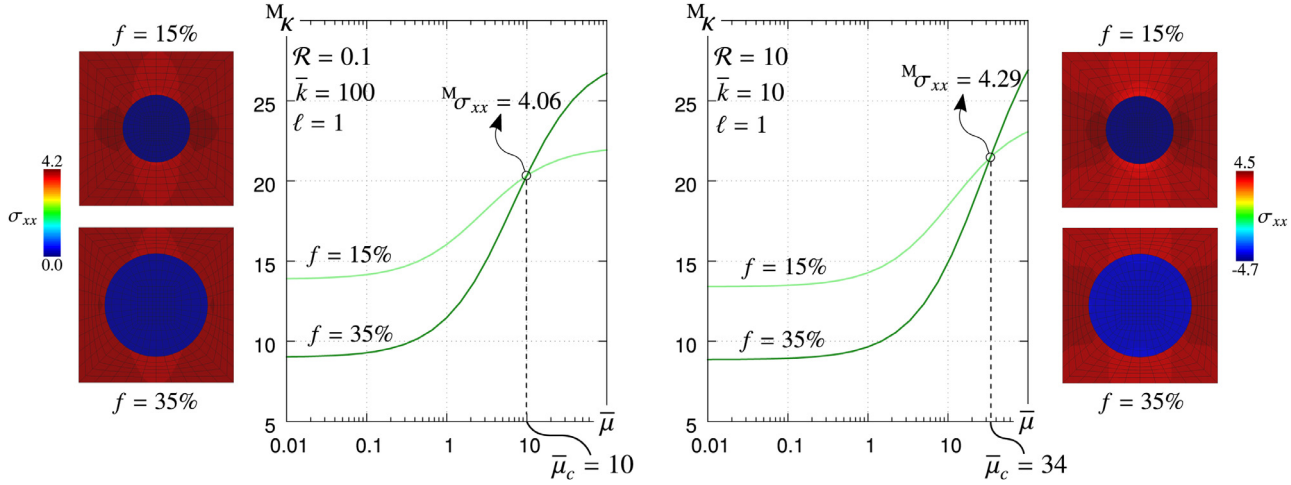

Fig. 6. Effective bulk modulus obtained for unit-cells with inclusion volume fractions $f = 15\%$ and $f = 35\%$ with respect to $\bar{\mu}$. The results confirm that for a particular value of $\bar{\mu}$, the effective response of the two unit-cells coincide. The figures next to the plots depict the distribution of the *xx*-component of the Cauchy stress within the microstructures for $\bar{\mu} = \bar{\mu}_c$ and two volume fractions.

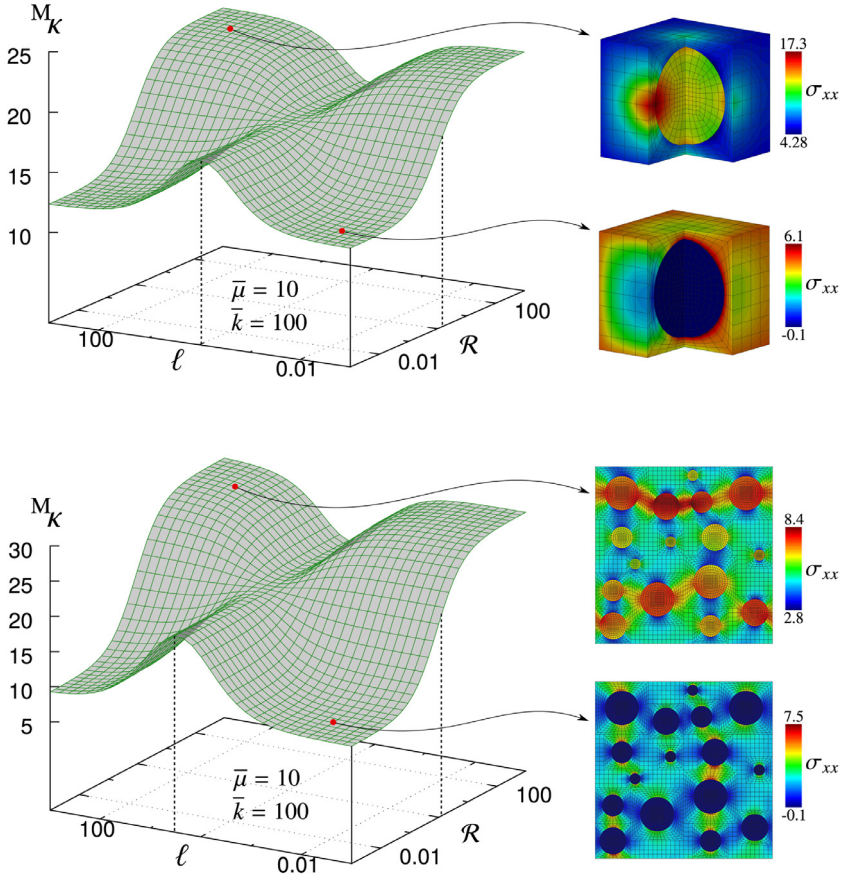

Fig. 7. Complex behavior of effective bulk modulus with varying the length-ratio and the inclusion to matrix stiffness-ratio obtained for a three-dimensional unit-cell and a two-dimensional microstructure with random distribution of inclusions possessing general interfaces. The figures next to the plot represent the distribution of the *xx*-component of the Cauchy stress within the microstructures for $\ell = 100$, $\mathcal{R} = 100$ (top) and $\ell = 0.01$, $\mathcal{R} = 0.01$ (bottom).

stiffness-ratio, the effective response becomes insensitive to the length-ratio ℓ.

4. Conclusion

In this manuscript, we analyzed the influence of size, inclusion to matrix stiffness-ratio and interface material parameters on the effective response of different microstructures equipped with general interfaces. The numerical results confirm that the behavior of the microstructure in the presence of a general interface, in contrast to other interface models, is nonintuitive and highly complex. Firstly, we demonstrated that depending on the size and the stiffness-ratio, the general interface model could lead to either a smaller-stronger or a smaller-weaker response. Next, it has been verified that for certain ranges of parameters, the general interface model results in a somewhat unexpected effective response. In

particular, for a certain size, the effective response becomes insensitive to the changes in the inclusion to matrix stiff ratio. Also, for a certain inclusion to matrix stiffness-ratio, the size effects vanish entirely. More surprisingly, we have found out that for particular values of interface parameters, the overall response remains unchanged even if the inclusion volume fraction is reduced. This behavior was observed for both a three-dimensional unit-cell as well as a two-dimensional microstructure.

In summary, we have reported on a number of unique, unprecedented and nonintuitive features of the effective behavior of materials in the presence of interfaces at their microstructures. We believe that the numerical observations in this manuscript reveal some of the previously unnoticed advantages of the general interface model and manifest its enormous potential to be considered as a powerful tool to design smart and multifunctional composites.

Acknowledgment

The support of this work by the Cluster of Excellence "Engineering of Advanced Materials" at the University of Erlangen–Nuremberg, funded by the DFG (EXC 315) within the framework of its "Excellence Initiative", is greatly appreciated.

References

Altenbach, H., Eremeyev, V., 2017. On the elastic plates and shells with residual surface stresses. Procedia IUTAM 21, 25–32.
Ansari, R., Gholami, R., 2016. Size-dependent modeling of the free vibration characteristics of postbuckled third-order shear deformable rectangular nanoplates based on the surface stress elasticity theory. Compos. Part B 95, 301–316.
Bargmann, S., Klusemann, B., Markmann, J., Schnabel, J., Schneider, K., Soyarslan, C., Wilmers, J., 2018. Generation of 3d representative volume elements for heterogeneous materials: a review. Prog. Mater. Sci. 96, 322–384.
Brassart, L., Inglis, H., Delannay, L., Doghri, I., Geubelle, P., 2009. An extended Mori–Tanaka homogenization scheme for finite strain modeling of debonding in particle-reinforced elastomers. Comput. Mater. Sci. 45, 611–616.
Cavalcante, M., Khatam, H., Pindera, M.-J., 2011. Homogenization of elastic-plastic periodic materials by FVDAM and FEM approaches - an assessment. Compos. Part B 42, 1713–1730.
Charalambakis, N., 2010. Homogenization techniques and micromechanics. A survey and perspectives. Appl. Mech. Rev. 63, 030803.
Chatzigeorgiou, G., Meraghni, F., Javili, A., 2017. Generalized interfacial energy and size effects in composites. J. Mech. Phys. Solids 106, 257–282.
Chen, Q., Wang, G., Pindera, M.-J., 2018. Homogenization and localization of nanoporous composites-a critical review and new developments. Composites 155, 329–368.
Cordero, N., Forest, S., Busso, E., 2016. Second strain gradient elasticity of nano-objects. J. Mech. Phys. Solids 97, 92–124.
Drago, A., Pindera, M.-J., 2007. Micro-macromechanical analysis of heterogeneous materials: macroscopically homogeneous vs periodic microstructures. Compos. Sci. Technol. 67, 1243–1263.
Drugan, W., Willis, J., 1996. A micromechanics-based non local constitutive equation and estimates of representative volume element size for elastic composites. J. Mech. Phys. Solids 44, 497–524.
Duan, H., Karihaloo, B., 2007. Thermo-elastic properties of heterogeneous materials with imperfect interfaces: generalized Levin's formula and Hill's connections. J. Mech. Phys. Solids 55, 1036–1052.
Eidel, B., Fischer, A., 2018. The heterogeneous multiscale finite element method for the homogenization of linear elastic solids and a comparison with the FE^2 method. Comput. Methods Appl. Mech. Eng. 329, 332–368.
Feyel, F., 1999. Multiscale FE^2 elastoviscoplastic analysis of composite structures. Comput. Mater. Sci. 16, 344–354.
Fritzen, F., Leuschner, M., 2015. Nonlinear reduced order homogenization of materials including cohesive interfaces. Comput. Mech. 56, 131–151.
Gurtin, M., Murdoch, A., 1975. A continuum theory of elastic material surfaces. Arch. Ration. Mech. Anal. 57 (4), 291–323.
Han, Z., Mogilevskaya, S., Schillinger, D., 2018. Local fields and overall transverse properties of unidirectional composite materials with multiple nanofibers and Steigmann-Ogden interfaces. Int. J. Solids Struct. 147, 166–182.
Hashin, Z., 2002. Thin interphase/imperfect interface in elasticity with application to coated fiber composites. J. Mech. Phys. Solids 50, 2509–2537.
He, J., Lilley, C., 2008. Surface effect on the elastic behavior of static bending nanowires. Nano Lett. 8, 1798–1802.
Hill, R., 1963. Elastic properties of reinforced solids: Some theoretical principles. J. Mech. Phys. Solids 11, 357–372.
Hill, R., 1972. On constitutive macro-variables for heterogeneous solids at finite strain. Proc. R. Soc. A 326, 131–147.
Jafari, A., Afaghi Khatibi, A., Mosavi Mashhadi, M., 2011. Comprehensive investigation on hierarchical multiscale homogenization using Representative Volume Element for piezoelectric nanocomposites. Composites 42, 553–561.
Javili, A., 2017. Variational formulation of generalized interfaces for finite deformation elasticity. Math. Mech. Solids 23, 1303–1322.
Javili, A., Chatzigeorgiou, G., Steinmann, P., 2013. Computational homogenization in magneto-mechanics. Int. J. Solids Struct. 50, 4197–4216.
Javili, A., Kässmair, S., Steinmann, P., 2014. General imperfect interfaces. Comput. Methods Appl. Mech. Eng. 275, 76–97.
Javili, A., Steinmann, P., Mosler, J., 2017. Micro-to-macro transition accounting for general imperfect interfaces. Comput. Methods Appl. Mech. Eng. 317, 274–317.
Kanit, T., Forest, S., Galliet, I., Mounoury, V., Jeulin, D., 2003. Determination of the size of the representative volume element for random composites: statistical and numerical approach. Int. J. Solids Struct. 40, 3647–3679.
Klusemann, B., Böhm, H., Svendsen, B., 2012. Homogenization methods for multi-phase elastic composites: Comparisons and benchmarks. Eur. J. Mech. 34, 21–37.
Kochmann, D., Wulfinghoff, S., Reese, S., Svendsen, B., Ehle, L., Mayer, J., 2017. Efficient and accurate two-scale FE-FFT-based prediction of the effective material behavior of elasto-viscoplastic polycrystals. Comput. Mech. 61, 751–764.
Maleki Moghadam, R., Saber-Samandari, S., Hosseini, S., 2016. On the tensile behavior of claye-epoxy nanocomposite considering interphase debonding damage via mixed-mode cohesive zone material. Composites 89 (303-315).
Matouš, K., Geers, M., Kouznetsova, V., Gillman, A., 2017. A review of predictive nonlinear theories for multiscale modeling of heterogeneous materials. J. Comput. Phys. 330, 192–220.
Miehe, C., 2002. Strain-driven homogenization of inelastic microstructures and composites based on an incremental variational formulation. Int. J. Numer. Methods Eng. 55, 1285–1322.
Moës, N., Cloirec, M., Cartraud, P., Remacle, J.-F., 2003. A computational approach to handle complex microstructure geometries. Comput. Methods Appl. Mech. Eng. 192, 3163–3177.
Mura, T., Shodja, H., Hirose, Y., 1996. Inclusion problems. Appl. Mech. Rev. 49, 118–127.
Nemat-Nasser, S., Hori, M., 1999. Micromechanics: Overall Properties of Heterogeneous Materials. Elsevier.
Ortiz, M., Pandolfi, A., 1999. Finite-deformation irreversible cohesive elements for three-dimensional crack-propagation analysis. Int. J. Numer. Methods Eng. 44, 1267–1282.
Ostoja-Starzewski, M., 2006. Material spatial randomness: From statistical to representative volume element. Probabilistic Eng. Mech. 21, 112–132.
Park, H., Klein, P., Wagner, G., 2006. A surface Cauchy-Born model for nanoscale materials. Int. J. Numer. Methods Eng. 68, 1072–1095.
Park, K., Paulino, G., 2013. Cohesive zone models: a critical review of traction-separation relationships across fracture surfaces. Appl. Mech. Rev. 64 (6), 060802.
Pavanello, F., Manca, F., Luca Palla, P., Giordano, S., 2012. Generalized interface models for transport phenomena: unusual scale effects in composite nanomaterials. J. Appl. Phys. 112, 084306.
Pindera, M.-J., Khatam, H., Drago, A.S., Yogesh, B., 2009. Micromechanics of spatially uniform heterogeneous media: a critical review and emerging approaches. Compos. Part B 40, 349–378.
Ponte Castañeda, P., 1992. New variational principles in plasticity and their application to composite materials. J. Mech. Phys. Solids 40, 1757–1788.
Quang, H., He, Q.-C., 2007. Size-dependent effective thermoelastic properties of nanocomposites with spherically anisotropic phases. J. Mech. Phys. Solids 55, 1899–1931.
Saeb, S., Steinmann, P., Javili, A., 2016. Aspects of computational homogenization at finite deformations: a unifying review from Reuss' to Voigt's bound. Appl. Mech. Rev. 68 (5), 050801.
Savvas, D., Stefanou, G., Papadrakakis, M., Deodatis, G., 2014. Homogenization of random heterogeneous media with inclusions of arbitrary shape modeled by XFEM. Comput. Mech. 54, 1221–1235.
Schröder, J., Keip, M.-A., 2012. Two-scale homogenization of electromechanically coupled boundary value problems. Comput. Mech. 50, 229–244.
Steigmann, D., Ogden, R., 1999. Elastic surface-substrate interactions. Proc. R. Soc. A 455, 437–474.
Temizer, İ., Wriggers, P., 2011. Homogenization in finite thermoelasticity. J. Mech. Phys. Solids 59, 344–372.
Tran, A., Le Quang, H., He, Q.-C., 2016. Computation of the size-dependent elastic moduli of nano-fibrous and nano-porous composites by FFT. Compos. Sci. Technol. 135, 159–171.
Tsalis, D., Chatzigeorgiou, G., Charalambakis, N., 2012. Homogenization of structures with generalized periodicity. Composites 43, 2495–2512.
Wilmers, J., McBride, A., Bargmann, S., 2017. Interface elasticity effects in polymer–filled nanoporous metals. J. Mech. Phys. Solids 99, 163–177.
Xu, X.-P., Needleman, A., 1994. Numerical simulations of fast crack growth in brittle solids. J. Mech. Phys. Solids 42, 1397–1434.
Yvonnet, J., He, Q.-C., Toulemonde, C., 2008a. Numerical modelling of the effective conductivities of composites with arbitrarily shaped inclusions and highly conducting interface. Compos. Sci. Technol. 68, 2818–2825.
Yvonnet, J., Quang, H., He, Q.-C., 2008b. An XFEM/level set approach to modelling surface/interface effects and to computing the size-dependent effective properties of nanocomposites. Comput. Mech. 42 (1), 119–131.